Heliyon 9 (2023) e15887

Contents lists available at ScienceDirect

Heliyon

journal homepage: www.cell.com/heliyon

Research article

Assessment of microstructure, nanomechanical and tribological properties of Ti-xNi alloys fabricated by spark plasma sintering

Azeez Lawan Rominiyi [a,*], Peter Madindwa Mashinini [a]

[a] Department of Mechanical and Industrial Engineering, University of Johannesburg, Doornfontein Campus, Johannesburg 2028, South Africa

ARTICLE INFO

Keywords:
Spark plasma sintering
Ti-xNi alloys
Nanoindentation
Wear performance
Ti_2Ni intermetallic

ABSTRACT

This work employed the nanoindentation and conventional dry sliding wear techniques to study the nanomechanical and tribological properties of the spark plasma sintered Ti-xNi (x = 2, 6 and 10 wt%) alloys. The microstructure and phase composition of the fabricated alloys were studied. The results indicated the presence of hexagonal close-packed (hcp) α-Ti and face-centred cubic (fcc) Ti_2Ni intermetallic phases within the matrix of the Ti-xNi alloys. Nanoindentation measurements under varying loads showed that the hardness (H), elastic modulus (E_r) and elastic recovery index (W_e/W_t) of the developed alloys increased with increasing nickel contents. At a constant load, the hardness trend aligns perfectly with the indentation size effect phenomenon. The H and E_r decreased upon transition from lower to higher loads. The H/E_r and H^3/E_r^2 ratios obtained from nanoindentation are higher for Ti-xNi alloys compared to pure Ti. This shows that the Ti-xNi alloys possessed better anti-wear characteristics than pure Ti. The wear analysis results show that the wear resistance increased with increasing volume fraction of the Ti_2Ni intermetallics in the sintered samples. Ti–10Ni alloy displayed the best nanomechanical and wear performances among the sintered samples.

1. Introduction

Commercially pure Ti displays exceptional properties that improve its utilization for many applications such as in marine, biomedical, aerospace and automobile industries [1–3]. The high specific strength of pure titanium, unlike nickel alloys and steel, makes it a material of choice for structural applications where weight is of critical consideration. Notwithstanding the unique qualities of titanium, titanium and its alloys are experiencing low patronage due to the high cost of extracting the metal from its ore and the high production cost stemming from the primary production method of casting. This is usually followed by secondary operations and finishing processes. The summation of these costs renders the titanium part very expensive compared to other structural metals [4,5].

The advent of powder metallurgy has seen researchers and materials engineers developing a keen interest in titanium and its alloys due to the capability of this process to produce a near-net-shape object, thereby removing the need for secondary operation after fabrication and preventing sample wastage [6,7]. This tremendously reduces the cost of producing titanium parts. Powder metallurgy processes such as hot pressing (HP) and hot isostatic (HIP) methods have been established in the literature to yield fully densified titanium parts. Nevertheless, these processes also increased the cost of production of Ti parts due to the high operating temperature and time required during pressing [8,9]. Aside from this, the conventional sintering process also retains pores within the matrix of the

* Corresponding author. Department of Mechanical and Industrial Engineering, University of Johannesburg, Doornfontein Campus, Johannesburg 2028, South Africa.
E-mail address: rominiyipedi@gmail.com (A.L. Rominiyi).

https://doi.org/10.1016/j.heliyon.2023.e15887
Received 20 December 2022; Received in revised form 19 April 2023; Accepted 25 April 2023
Available online 2 May 2023

sintered samples, leading to poor microstructural characteristics and mechanical properties of the developed parts. However, spark plasma sintering (SPS) has been reported as a novel powder metallurgy technique capable of producing fully densified samples at relatively lower sintering temperature and time [10,11]. Thus, solving the problem associated with conventional processing methods.

Nanoindentation technique is an appropriate method which has been used on several occasions by researchers to determine the hardness and elastic modulus of different materials [12–14] from microscale to nano-scale level [15,16]. Aside from this, nanoindentation technique is used to conduct in-situ properties assessment of materials without unsettling their microstructural characteristics. The technique places no restriction on the configuration of the testing materials [17,18]. Despite the enviable benefits of the nanoindentation technique, the testing material experiences non-uniform total stress because the indentation deformation restricts the flow of the material from the immediate area. Thus, it is challenging to evaluate the stress-strain characteristics of material from the indentation made by the pointed-end Berkovich indenter [19]. The importance of nanoindentation stretches beyond evaluating nanohardness and elastic modulus of materials. According to Fornell et al. [20], this method has effectively been used to assess other variables which can aid accurate predictions of the durability of a part in service.

Ti–Ni alloys have found applications as thermomechanical actuators, heat-sensitive elements and hydrogen storage tanks for satellite propulsion due to their cryogenic properties. Their high specific resistance and low density make them materials of choice in naval construction and the automotive industry [21–23]. Previous works have reported the bulk properties of Ti–Ni alloys containing minor additions of elemental nickel. Panigrahi [24] found that the addition of nickel to titanium using dilatometric sintering lowered the activation energies of titanium, thereby facilitating increased Ti–Ni inter-diffusion and Ti–Ti self-diffusion in the matrix. Consequently, this resulted in improved sinterability of titanium. Robertson and Schaffer [25] studied the suitability of nickel as an alloying element for titanium. Low et al. [26] reported on the role played by the nature of the starting powder. They found that using titanium powder produced through the Hydride-mill–dihydride (HDH) method caused excessive porosity and expansion of the sample during the liquid phase sintering due to the release of hydrogen within the pores of the sintered compacts. However, Robertson and Shaffer [27], in their work on dilatometry sintering of Ti–Ni, posited that the use of low pressing pressure and shorter duration of sintering is the panacea to swelling of the compact experienced during liquid phase sintering of titanium binary alloys. Liu et al. [28] employed the press and sinter method during the liquid phase sintering of Ti–Ni binary alloys containing small nickel additions. The authors reported an improvement in the bulk properties of the sintered alloys.

Though, during the application of materials in service, components interact through the contacting surfaces. The reviewed literature showed ample information on the bulk properties of Ti-xNi alloys containing minor nickel additions with little attention given to the surface properties of the alloys. Thus, making it imperative to study the surface properties of the developed materials. According to Musil et al. [29] and Leyland and Mathews [30], nanoindentation technique is an efficient method for evaluating the surface properties of materials. Hence, in this work, the surface properties of the developed Ti-xNi alloys were investigated using nanoindentation and conventional wear techniques to further knowledge on the properties of these alloys and widen the areas of application of titanium-based components.

2. Methodology

2.1. Fabrication of Ti-xNi alloys

In this work, the starting materials consist of pure Ti powder, grade 1 (Fig. 1a), with particle size less than 25 μm; 99.8% purity; Ni powder (Fig. 1b) having a particle size of less than 0.3 μm; 99.5% purity. The powders were supplied by TLS Technik, Germany and Weartech (pty) Ltd, South Africa. The Ti-xNi alloys (x = 2 wt%, 6 wt% and 10 wt%) were mixed in a Turbula mixer (TF2, WAB Switzerland) under a rhythmic, three-dimensional motion for 8 h at 101 revolutions per minute to ensure uniform mixing of the constituents (Fig. 1c: Stage I). The properly mixed powder was weighed appropriately and poured into a 20 mm diameter graphite-sheet-lined die to produce a disc of dimension 20 mm × 10 mm. The die-punch assembly was placed in the SPS furnace (FCT Systeme, H-HPD 25, Germany), and sintering was conducted under constant sintering parameters of 850 °C, 100 °C/min, 50 MPa for 10 min in a vacuum atmosphere of <4 Pa (Fig. 1d: Stage II). The sample was allowed to cool to room temperature in the SPS furnace, after

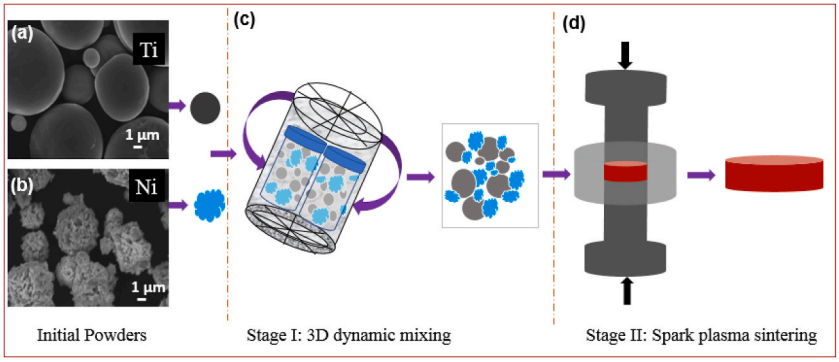

Fig. 1. SEM images of the initial powders (a and b) and schematic illustration of the fabrication process of Ti-xNi alloys (c and d).

which it was removed and sandblasted to remove any form of carbon contamination on the sample's surface. The relative density of the sintered samples was determined by the Archimedes' method using distilled water as the immersion medium. The relative density of the sintered Ti-xNi alloys was obtained with reference to the theoretical bulk density of the green samples (Equation (1)) and average value after six measurements was recorded for each sample. The metallographic samples were ground and polished to mirror finish and etched using Kroll's reagent before microstructural and phase analysis using a field electron scanning electron microscope (Zeiss Ultra Plus 55, FESEM) equipped with EDS detector suite (INCA X-Stream 2 pulse analyser software) and X-ray diffractometer (PW 1710, PANalytical Empyrean) using Cu Kα monochromatic radiation (λ = 0.15406 nm) having a reflection geometry of 2θ between 5° and 90°.

$$(\rho_{bulk})^{-1} = \left(\frac{\text{wt.\%Ti}}{\rho_{\text{Ti}}} + \frac{\text{wt.\%Ni}}{\rho_{\text{Ni}}}\right) \tag{1}$$

where, ρ_{bulk}, ρ_{Ti} and ρ_{Ni} are bulk density of the green compact, density of Ti and density of Ni, respectively.

2.2. Nanoindentation test

The fabricated samples were sectioned into specimens with dimension 10 mm × 10 mm x 5 mm and polished to mirror finish following ASTM E3-11. Then, the nanoindentation properties of the sintered samples were studied using a Nanoindenter system (Anton-Parr TTX-NHT3, Germany) equipped with a standard, triangular pyramid, Berkovich diamond indenter. This indenter is preferred for hardness and modulus measurement as it can be ground to a sharp point easily [31]. The equipment was calibrated with a standard specimen made of fused Silica prior to the commencement of the investigation. The test was conducted by making an impression on the polished surface of the specimen under an applied load ranging from 50 mN–150 mN at an interval of 50 mN. The loading rate and dwell time were maintained at 150 mN/min and 20 s. The equipment dynamically recorded the applied load and displacement data as a function of time. The equipment was configured in accordance with ISO 14577 standard [32]. Following the Oliver and Pharr method [33], the resulting nanoindentation properties of the analyzed samples are depicted in this work.

According to Oliver and Pharr [33], the nanohardness of the investigated sample can be obtained using Equation (2).

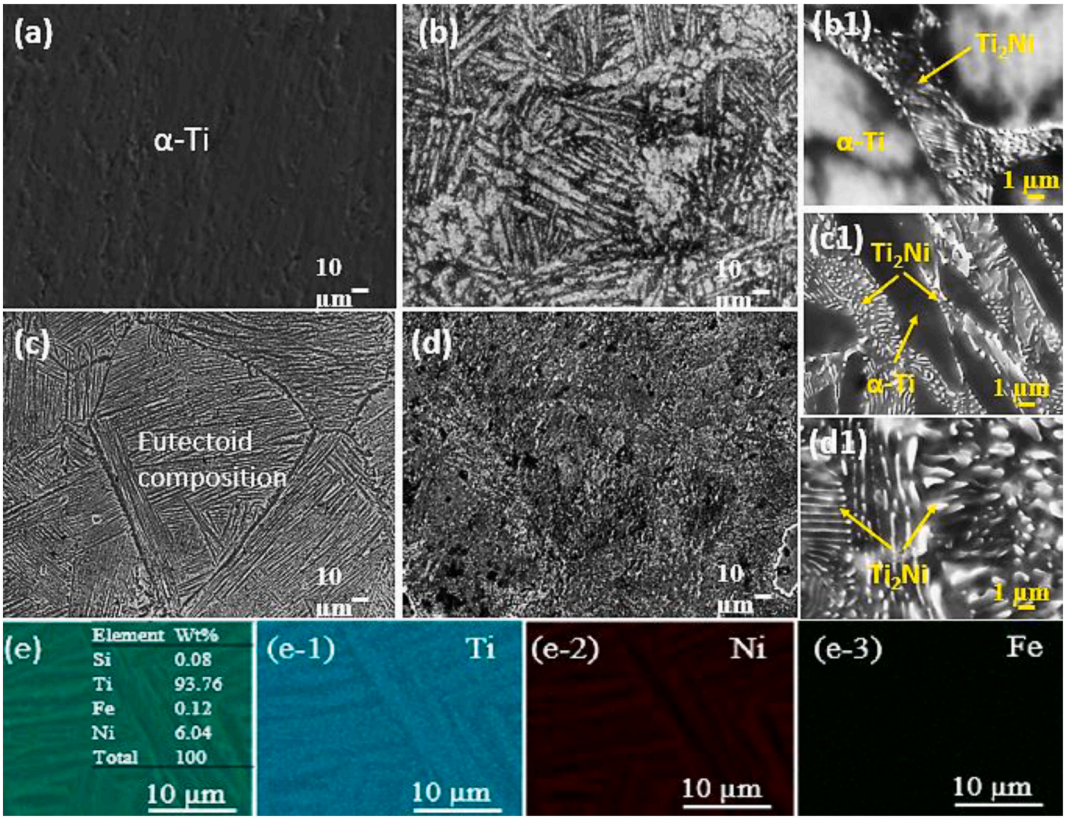

Fig. 2. SEM images of (a) pure Ti (b) Ti–2Ni (c) Ti–6Ni (d) Ti–10Ni; Higher magnification SEM image of (b1) Ti–2Ni (c1) Ti–6Ni (d1) Ti–10Ni; (e) EDS layered image confirming the elemental composition of Ti–6Ni and (e-1)–(e-3) showing the elemental distribution in (e).

$$H = \frac{P_{max}}{A_c} \tag{2}$$

where H is nanohardness, P_{max} is the highest load and A_c is the indentation area. The area of indentation is defined by Equation (3) as:

$$A_c = P\left(h_c^2\right), \tag{3}$$

where P is the applied load and h_c is the contact depth at maximum load.

Equation (4) presents the expression for the reduced elastic modulus, E_r.

$$\frac{1}{E_r} = \frac{1-v^2}{E} + \frac{1-v_i^2}{E_i} \tag{4}$$

where E_i = Berkovich indenter modulus (0.07), v_i = Poisson's ratio (1141 GPa) [34], E = sample's modulus and v = sample's poisson's ratio.

Furthermore, a universal tribometer, Rtec, MFT- 5000, configured in reciprocating ball-on-flat mode and operated following the ASTM G133 standard, was used to conduct the dry sliding wear test at room temperature using a universal tribometer. The pure Ti and Ti-xNi samples (10 × 10 × 4 mm) were subjected to the reciprocating motion of the counterface ball (Ø 6.35 mm) over a sliding distance of 5 mm for 30 min at a constant load of 35 N. The sliding speed of 4 mm/s was maintained throughout the test. Subsequently, the coefficient of friction (COF) and specific wear rate of the samples were evaluated. The worn surface of the samples was investigated using SEM (JEOL JSM-7600F).

3. Results and discussion

3.1. Microstructure and phase composition of the fabricated samples

Fig. 2 presents the SEM images and EDS results of the developed pure Ti and Ti-xNi alloys. The microstructure of the pure Ti in Fig. 2a showed the predominance of single phase as sintering was conducted at 850 °C, the β-transus temperature of pure titanium (915 °C) [35]. This single phase was suggested to be the room temperature allotropy (α-Ti) of pure Ti. The XRD results in Fig. 3 confirmed the predominant phase in the pure Ti as the α-Ti, hcp phase. The addition of 2 wt% of Ni to the pure Ti (Fig. 2b) revealed the coexistence of white acicular structures within the dark, α-Ti-dominated matrix of the pure Ti (Fig. 2(b1)). The EDS elemental analysis of these acicular features showed the presence of Ti and Ni. This was due to the occurrence of a eutectoid reaction between the titanium matrix and the nickel additives and the formation of Ti_2Ni intermetallic [24,25,36]. Microstructural features similar to that observed in Ti–2Ni alloy were seen in Ti–6Ni (Fig. 2c and c1) and Ti–10Ni (Fig. 2d and d1) alloys due to the increasing interactions between the matrix and the nickel additives, leading to the formation of more acicular structures within the matrix. The high magnification SEM images in Fig. 2(b1–d1) revealed clearly that the Ti_2Ni intermetallic fractions within the alloy's matrix increased with increasing nickel content. The EDS layered mapping of the Ti–6Ni sample in Fig. 2e confirmed the elemental composition of this alloy. Figs. 2(e-1)–(e-3) showed the uniform dispersion of the elemental constituents within the Ti-6Ni alloy matrix. The EDS mapping result also indicated the existence of other trace elements, such as Si and Fe (Fig. 2e and (e-3)), with no noticeable influence on the phase evolution due to their insignificant fraction in the initial pure Ti powder.

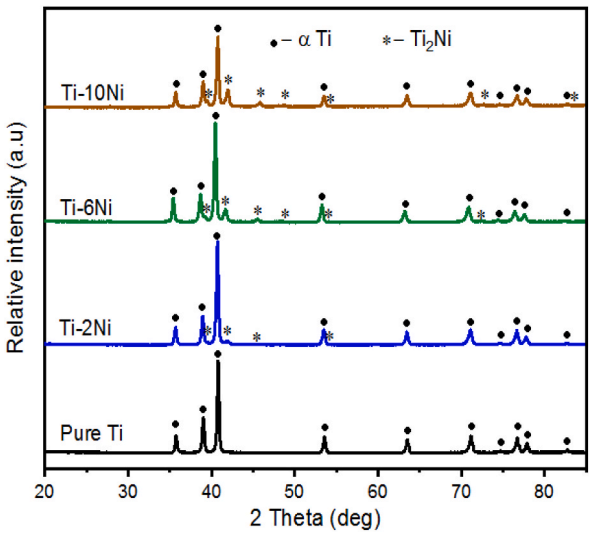

Fig. 3. XRD diffractograms of sintered samples.

The microstructure of the sintered samples also revealed that fully densified samples with relative densities above 99% were fabricated (Table 1). This can be traced to the combining effect of electric, temperature, and stress fields generated during fabrication in the SPS furnace [37]. Moreover, the ability of nickel to lower the activation energy of titanium and promotes atomic diffusion and phase formation, eliminates pores and enhances metallurgical bonding between adjacent particles, increased densification with increasing nickel contents in the fabricated Ti-xNi alloys [36,38] as observed in Table 1.

Fig. 3 shows the XRD patterns, which revealed the phase distribution in the sintered pure Ti and Ti-xNi samples. The diffractogram of the pure Ti indicated a predominant hcp, α-Ti phase with lattice parameters a = b = 2.9440 Å, c = 4.6780 Å. However, with the addition of 2, 6 and 10 wt% Ni, the decreasing intensity of the α-Ti was observed. The emergence of small peaks of Ti_2Ni intermetallic phase (fcc), which can be attributed to the lower fraction of the Ti_2Ni intermetallic phase present in the Ti–2Ni alloy (Table 1), were observed in diffraction pattern of Ti–2Ni alloy. These peaks become more pronounced at higher nickel contents of 6 and 10 wt%. The Ti_2Ni intermetallic phase was formed within the matrix of the Ti-xNi alloys because the presence of nickel lowers the activation energy of titanium and enhances its diffusion [36,39]. Thus, creating a favourable condition for the eutectoid reaction between the titanium matrix and the nickel additive.

Furthermore, Ni, being a β-Ti stabilizer, dissolves to a great extent in the β-Ti, forming a solid solution in β-Ti. The unstable β-Ti decomposes upon cooling to form Ti_2Ni intermetallic phase observed in the Ti-xNi matrix (Fig. 3). Also, the fact that the $\Delta G_{Ti2Ni} < 0$ ($\Delta G_{Ti2Ni} = -49{,}120 + 17.208\ T$ (J/mol)) encourages the spontaneous formation of Ti_2Ni [40] within the matrix of the alloy. The increasing diffraction peaks of the Ti_2Ni intermetallic phase (Fig. 3) correlate with its growing concentration at the expense of the α-Ti phase within the matrix of the sintered alloys, as shown in Table 1. Ti_2Ni intermetallic being a hard phase with higher hardness and elastic modulus [41] than the matrix, induce microstrain within the matrix and enhance the deformation resistance of the Ti-xNi alloys.

3.2. Nanoindentation properties of the SPSed samples

3.2.1. Nanoindentation load vs penetration depth and penetration depth vs time curves

The nanoindentation load-penetration depth curves of the sintered pure Ti and Ti-xNi alloys under varied indentation loads are presented in Fig. 4a–c. Generally, the shapes of the curves depict no crack formation on the surface of the samples during the downward movement of the indenter tip into the samples. It was also observed that all the samples displayed initial resistance to the penetration of the indenter tip. This behaviour was attributed to the pop-in effect caused by dislocation nucleation and pile-ups underneath the indenter tip and around the grain boundaries of the alloys [42,43]. Besides the elastic-plastic transition features observed in Fig. 4a–c, the curves further showed increasing penetration depth with increasing applied indentation loads. The pure Ti and Ti–10Ni samples displayed the maximum and minimum penetration depth across the applied loads. Therefore, the shallow penetration depths obtained in Ti-xNi alloys signified improved stiffness and resistance to plastic deformation with increasing nickel content.

Similarly, Fig. 5a–c shows the variation of the penetration depth of the sintered pure Ti and Ti-xNi alloys as a function of the test duration. It can be observed that the penetration depth reduces with increasing nickel content in the tested samples, as shown in Fig. 5a–c. Thus, at an applied load of 50 mN, 100 mN and 150 mN, pure Ti exhibited the highest penetration distance of 705 nm, 1179 nm and 1728 nm, respectively. In contrast, the least penetration depths of 382 nm, 920 nm, and 1047 nm were exhibited by the sintered Ti–10Ni sample under similar conditions. This is an indication that nickel addition enhanced the resistance of the indented samples to plastic deformation due to dislocation formation and multiplication [44,45]. Propagation of the generated dislocations was restricted by the existence of the hard, Ti_2Ni intermetallic phase within the matrix of the Ti-xNi alloys. At higher nickel content, more Ti_2Ni phase is formed within the matrix, which translates to increasing impediments to dislocation movements and decreasing penetration depth.

3.2.2. Nanomechanical properties

The variation of the nanohardness and the elastic modulus values of the fabricated samples across the applied loads are presented in Fig. 6a and b, respectively. Fig. 6a shows that the nanohardness values of the sintered samples increase with growing nickel fraction in the Ti-xNi alloys. The nanohardness values of the sintered samples was seen to decrease gradually as the indentation load increased from 50 mN to 150 mN. The pure Ti sample demonstrated the least nanohardness values of 4418 MPa, 3695 MPa and 2546 MPa at a corresponding load of 50 mN, 100 mN and 150 mN, respectively. On the contrary, the sintered Ti-xNi samples showed improved properties, with the Ti–10Ni sample exhibiting the highest nanohardness values of 10,467 MPa, 8072 MPa and 7497 MPa under 50 mN, 100 mN and 150 mN indentation loads, correspondingly.

Expectedly, the reduced elastic modulus values in Fig. 6b indicated that the pure Ti demonstrated the lowest reduced elastic

Table 1
Phase distribution and relative density of the sintered pure Ti and Ti-xNi alloys.

	Volume fraction of phases		
Sintered samples	α-Ti (%)	Ti_2Ni (%)	Relative density (%)
Pure Ti	100		99.3 ± 0.19
Ti–2Ni	91	9	99.42 ± 0.13
Ti–6Ni	76	24	99.78 ± 0.08
Ti–10Ni	62	38	99.82 ± 0.12

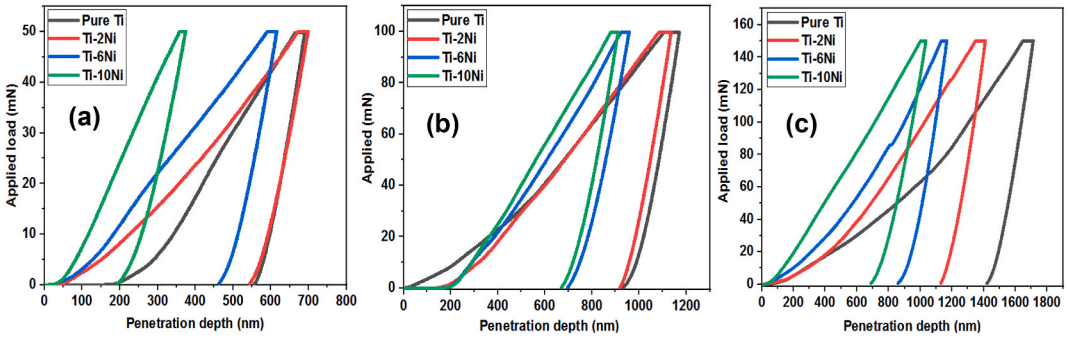

Fig. 4. Applied load-penetration depth graphs of the sintered samples under varied loads (a) 50 mN (b) 100 mN (c) 150 mN.

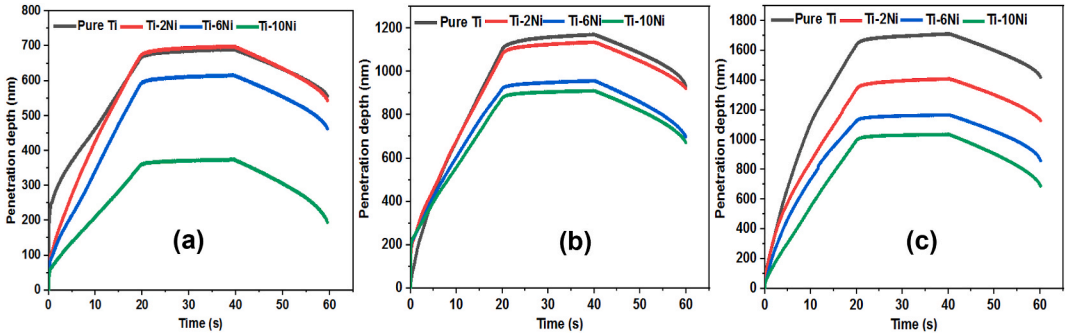

Fig. 5. Nanoindentation penetration depth vs time graphs of the sintered samples under varied loads (a) 50 mN (b) 100 mN (c) 150 mN.

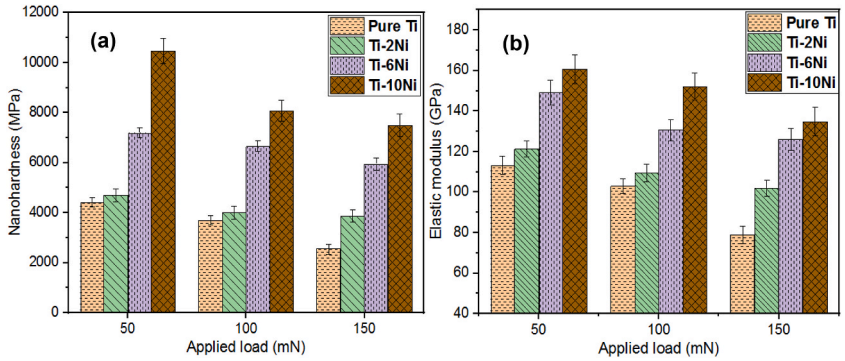

Fig. 6. (a) Nanohardness and (b) reduced elastic modulus under different nanoindentation loads.

modulus across the applied loads. The elastic modulus obtained in this work for pure Ti under the least load agrees with the elastic modulus (115 GPa and 112 GPa) reported by Dekhil et al. [46] and Abdi et al. [47] while evaluating the nanoindentation properties of pure Ti. Ti–10Ni sample exhibited the highest reduced elastic modulus of 160.75 GPa, 152.12 GPa and 134.85 GPa under a respective load of 50 mN, 100 mN and 150 mN. The elastic modulus values obtained in this work fall within limits (130.73 GPa–164.53 GPa) specified in the literature for sintered Ti–Ni alloy [46]. The nanohardness and elastic modulus trends across the loads as observed in Fig. 6 can be ascribed to the fact that contact area and plastic deformation significantly increase with increasing load [48]. Thus, the increasing penetration depth observed as the load transit from low-load to high-load conditions, corresponds to decreasing hardness of the material. This behaviour contradict the typical plasticity theory in which the hardness of material maintains a constant value regardless of the indentation depth in the sample but aligns perfectly with the indentation size effect phenomenon [49–51], as at a given load, an inverse relationship exists between the hardness and depth of penetration witnessed by the samples. Since a proportional relationship exists between hardness and the elastic modulus of a material [52], hence the similar trend observed in the elastic modulus of the materials (Fig. 6b). Also, the precipitation of hard, Ti_2Ni intermetallic phase, which according to Wang et al. [41], possesses higher hardness and elastic modulus but a lower plastic factor translates to enhanced resistance to dislocation propagation in the Ti-xNi alloys. Dislocation interactions and pile-ups at grain boundaries (Orowan strengthening) within the material result in

strain-hardening under a particular load. According to Thornby et al. [49], this subsequently increases the hardness and elastic modulus of the samples under a particular load with increasing nickel content in the sintered alloys as observed in Fig. 6.

3.2.3. Wear properties

Fig. 7 shows the variation of the yield strain, $\left(H/E_r\right)$ and yield pressure, $\left(H^3/E_r^2\right)$ of the sintered pure Ti and Ti-xNi samples under different applied loads. In Fig. 7a, the yield strain was observed to increase with increasing nickel content across the applied indentation loads. A noticeable improvement in the yield strain and the yield pressure of the sintered Ti-xNi binary alloys was observed in Fig. 7a and b compared to the sintered pure Ti. The pure Ti exhibits the lowest yield strain of 0.039, 0.035, and 0.032, accompanied by the least yield stress of 0.0057 GPa, 0.0047 GPa, and 0.0026 GPa under an applied load of 50 mN, 100 mN and 150 mN. Conversely, the sintered Ti–10Ni sample indicates the highest yield strain of 0.065, 0.053 and 0.056, with the highest yield pressure of 0.0444 GPa, 0.0227 GPa and 0.0232 GPa across the corresponding indentation loads of 50 mN, 100 mN and 150 mN.

The conventional theory of wear revealed that hardness plays a significant role in the wear behaviour of a material [53,54]. Consequently, materials with a high hardness value display high yield strain $\left(H/E_r\right)$ otherwise referred to as the resistance to elastic strain to failure, and high yield pressure $\left(H^3/E_r^2\right)$, which represents the plastic deformation resistance of the material, exhibits high wear and plastic deformation resistance during nanoindentation [54,55], respectively. Several reports in the literature [13,14,20, 54–56] have established that the higher the yield strain $\left(H/E_r\right)$ and yield pressure $\left(H^3/E_r^2\right)$ of a material, the higher its resistance to wear and plastic deformation. Hence, the results in Fig. 7 demonstrate that the sintered Ti-xNi alloys displayed better wear resistance compared to pure Ti, with the Ti–10Ni sample possessing the best anti-wear properties among the sintered samples.

The elastic recovery index, $\left(W_e/W_t\right)$ and the plasticity index, $\left(W_p/W_t\right)$ are other parameters that greatly influence the mechanical performance of a component. According to Hynowska et al. [57] and Ehtemam-Haghighi et al. [13], the elastic recovery and plasticity index represent the resistance of a material to impact and the intrinsic plasticity of an alloy, respectively. Fig. 8 illustrates the results of the elastic recovery and plasticity index of the fabricated samples across the applied loads.

Fig. 8a indicates that the elastic recovery index of the developed samples increases with rising nickel content under each applied load. Pure Ti showed the lowest elastic recovery index, while Ti–10Ni alloy yielded the highest elastic recovery index. The elastic recovery index of the Ti–10Ni alloy increased by about 92.4%, 65.2% and 65.9% across the applied loads compared to the pure Ti. However, a decreasing trend of the plasticity index (Fig. 8b) at a particular load was observed with increasing hardness of the sintered alloys. Therefore, Ti–10Ni, the hardest of the sintered samples (Fig. 6a), displayed the least plasticity, which was approximately 15.7%, 14.1% and 14.0% lower than that of the pure Ti across the indentation loads. Since the sintered Ti-xNi alloys demonstrated better elastic and poorer plasticity index compared to the pure Ti (Fig. 8), this suggests that they possessed higher impact loading resistance [13,56,58], with the Ti–10Ni sample being the best among the sintered Ti-xNi samples. The observed trends of the elastic recovery and plasticity index can be ascribed to the increase in fractions of hard, α-Ti and Ti_2Ni intermetallic phases, which invariably increase the hardness of the samples with a resultant declining ductility as the nickel content increases in the sintered samples.

Graphs depicting the coefficient of friction (COF) and average COF and wear rate of the samples are presented in Fig. 9a and b, correspondingly. Fig. 9a shows the oscillating profiles of the COF of the samples under an applied load of 35 N. The COF profile of the pure Ti exhibits the highest magnitude with less fluctuation compared to the Ti-xNi alloys due to the absence of a hard, Ti_2Ni intermetallic phase within its matrix. Conversely, the higher fluctuation COF profiles of the Ti-xNi alloys were observed due to the interaction of the sliding ball with the asperities created by the hard, Ti_2Ni phase within the Ti-xNi alloys [59]. Thus, pure Ti experienced the highest average COF and specific wear rate of 0.51 and 0.69 $\times$ 10^{-3} mm^3/Nm (Fig. 9b), respectively, during the sliding movement of the counterface ball. The increasing H/E_r and H^3/E_r^2 values of the Ti-xNi samples as the nickel content increase (Fig. 7) translates to enhanced wear resistance, as observed in Fig. 10b–c. Consequently, Ti–10Ni alloy exhibited the least average COF and specific wear rate of 0.34 and 0.22 $\times$ 10^{-3} mm^3/Nm, respectively. As shown in Fig. 9.

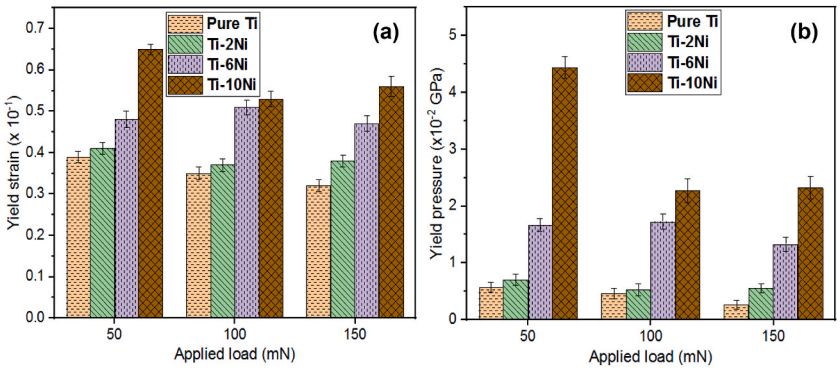

Fig. 7. (a) Yield strain (b) yield pressure across the different nanoindentation loads.

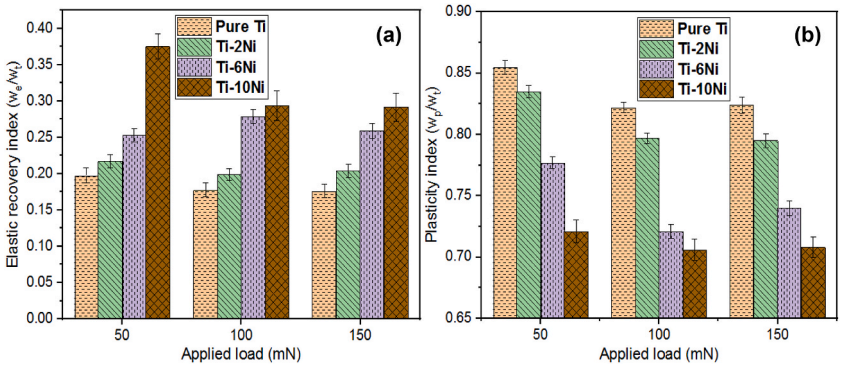

Fig. 8. (a) Elastic recovery index (b) plasticity index under varied loads.

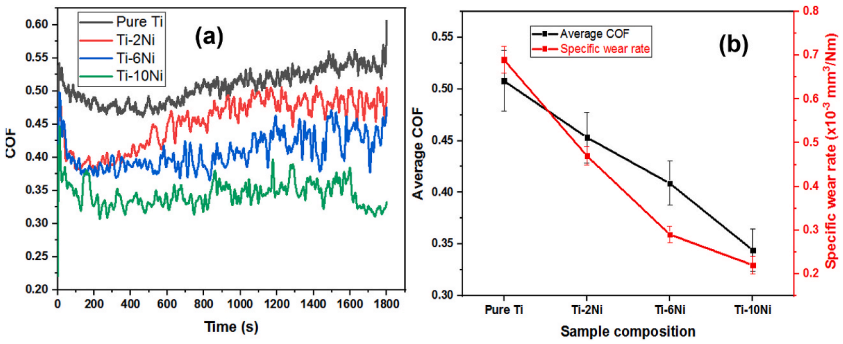

Fig. 9. (a) COF profile of the samples (b) variation of average COF and specific wear rate of the fabricated samples.

The SEM images in Fig. 10 show the wear scars of the fabricated samples. Generally, parallel grooves and delamination of varying degrees due to the sliding action of the counterface alloy steel ball were observed as the characteristic features of the worn surface. These features show the predominant wear mechanism to be that of the abrasive and adhesive wear due to the reciprocating action of the counter ball on the surface of the samples, which results in plastic deformation and micro-cutting of the soft pure Ti matrix [60]. However, the influence of the adhesive wear waned as the nanohardness of the sintered Ti-xNi alloys increased, as observed in Fig. 10b–d and the active wear mechanism at higher nickel contents was only that of abrasive wear. Therefore, the pure Ti with the lowest nanohardness compared to Ti-xNi samples (Fig. 6a) is susceptible to severe plastic deformation, which results in the observed pronounced grooves and delaminated regions on the worn surface (Fig. 10a). The wear characteristics of the sintered alloys can be attributed to the increasing fractions of the hard intermetallic phase in the pure Ti matrix which reduce the ductility of the contact area and results in increased resistance of the samples to the abrasive action of the counterface ball [59].

Furthermore, the insets of Fig. 10 show that the width of the wear track decrease with increasing nanohardness of the samples. This signifies growing resistance to the penetration of the counterface ball into the samples as the hardness of the materials increases. This observation aligns with the results of Archard's work on wear, reiterating the wear behaviour's dependency on the hardness of the material under investigation [61].

Ti–10Ni sample with the highest nanohardness (Fig. 6a) displayed a worn surface with shallow grooves without delamination (Fig. 10d), which can be traced to the increased resistance to plastic deformation, reduced surface roughness and abrasive effect of the counterface alloy. Hence, the lowest average COF and specific wear rate of 0.34 and 0.22 $\times$ 10^{-3} mm^3/Nm (lowest material loss) were obtained for the Ti–10Ni alloy among the investigated samples (Fig. 9b).

The results obtained from the sliding wear test of the sintered samples agree with the submissions from H/E_r and H^3/E_r^2 ratios found through the nanoindentation technique. Hence, the nanoindentation technique can give a true measure of the mechanical properties such as hardness, elastic modulus, and anti-wear characteristics of a material with a high-reliability level comparable to those obtained through the conventional mechanical and wear tests.

4. Conclusion

The microstructure, nanomechanical and tribological properties of the pure Ti and Ti-xNi binary alloys fabricated by spark plasma sintering were studied in this work. The predominance of the α-Ti phase was observed within the matrix of the pure Ti. Conversely, the Ti-xNi alloys contain a eutectoid composition of α-Ti and acicular Ti_2Ni intermetallic phases. The nanoindentation measurement

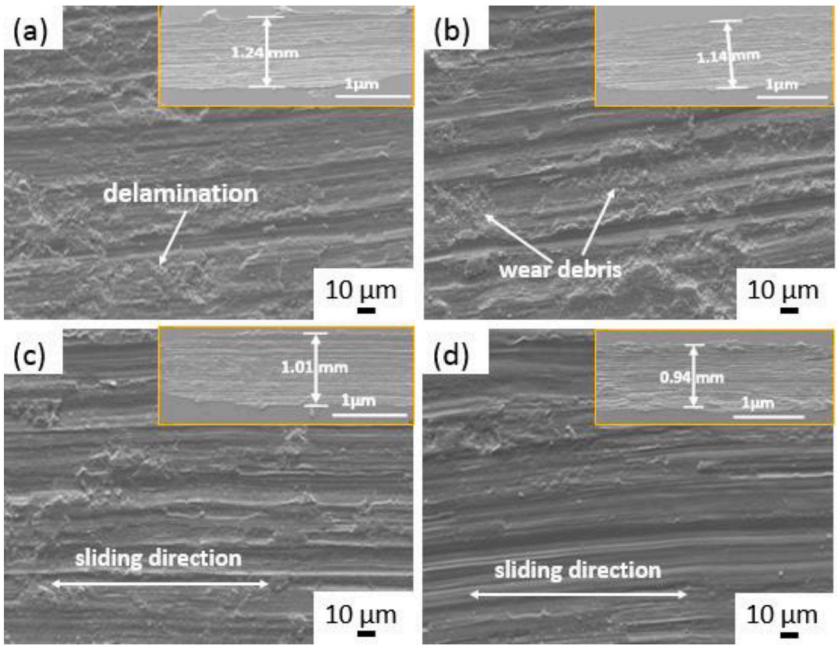

Fig. 10. SEM images of the worn surface of (a) Pure Ti (b) Ti–2Ni (c) Ti–6Ni (d) Ti–10Ni alloys.

indicated that the hardness, elastic modulus of the sintered samples varied with the indentation loads and were higher in Ti-xNi alloys compared to those of pure Ti. The enhanced H/E_r and H^3/E_r^2 values of the Ti-xNi alloys signify their superior wear resistance compared to the pure Ti. Also, a higher elastic recovery index (W_e/W_t) was observed for the Ti-xNi alloys, which implies their higher impact resistance compared to the pure Ti. The wear analysis results also showed improved wear resistance of the Ti-xNi than the pure Ti. Ti–10Ni sample exhibited the best performance among the sintered samples. This was ascribed to the highest fractions of the hard, Ti_2Ni intermetallic phase within the matrix of the Ti–10Ni sample. The outcome of this work shows that the tribological characteristics obtained through the nanoindentation technique are consistent with the dry sliding wear results of the sintered samples. Therefore, nanoindentation technique can be employed to predict the reliability of materials utilized for tribological applications.

Author contribution statement

Azeez Lawan Rominiyi, Peter Madindwa Mashinini: Conceived and designed the experiments; Performed the experiments; Analyzed and interpreted the data; Contributed reagents, materials, analysis tools or data; Wrote the paper.

Data availability statement

The raw/processed data required to reproduce these findings cannot be shared at this time as the data also forms part of an ongoing study.

Acknowledgement

The authors would like to acknowledge the support offered through the Global Excellence and Stature (GES) of the University of Johannesburg, Department of Mechanical and Industrial Engineering, South Africa. The Centre for Nanoengineering and Tribocorrosion (CNT), University of Johannesburg and Surface Engineering Research Laboratory (SERL), Tshwane University of Technology, South Africa are also appreciated for granting access to their research facilities.

References

[1] G. Lutjering, J.C. Williams, Titanium. Engineering Materials and Processes, Springer, Berlin, 2007.
[2] J.J. Noel, N. Ebrahimi, D.W. Shoesmith, Corrosion of titanium and titanium alloys, in: K. Wandelt (Ed.), Encyclopedia of Interfacial Chemistry, Elsevier, Oxford, 2018, pp. 192–200.
[3] M. Niinomi, Titanium alloys, in: Reference Module in Biomedical Sciences, Elsevier, 2018.
[4] D. Banerjee, J.C. Williams, Perspectives on titanium science and Technology, Acta Mater. 61 (3) (2013) 844–879.
[5] B.E. Hurless, F.H. Froes, Cost of titanium, AMPTIAC Q. 6 (2) (2002) 3–9.
[6] T.E. Norgate, G. Wellwood, The potential applications for titanium metal powder and their life cycle impacts, JOM 58 (9) (2006) 58–63.
[7] Z.Z. Fang, et al., Powder metallurgy of titanium – past, present, and future, Int. Mater. Rev. (2017) 1–53.

[8] C. Cai, et al., Effect of hot isostatic pressing procedure on performance of Ti6Al4V: surface qualities, microstructure and mechanical properties, J. Alloys Compd. 686 (2016) 55–63.
[9] H. El Kadiri, et al., Development of a Ti-based alloy: design and experiment, JOM 61 (5) (2009) 60–66.
[10] T. Borkar, et al., Reactive spark plasma sintering (SPS) of nitride reinforced titanium alloy composites, J. Alloys Compd. 617 (2014) 933–945.
[11] P. Cavaliere, B. Sadeghi, A. Shabani, Spark plasma sintering: process fundamentals, in: P. Cavaliere (Ed.), Spark Plasma Sintering of Materials: Advances in Processing and Applications, Springer International Publishing, Cham, 2019, pp. 3–20.
[12] Q. Liao, et al., A hybrid model to determine mechanical properties of soft polymers by nanoindentation, Mech. Mater. 42 (12) (2010) 1043–1047.
[13] S. Ehtemam-Haghighi, G. Cao, L.-C. Zhang, Nanoindentation study of mechanical properties of Ti based alloys with Fe and Ta additions, J. Alloys Compd. 692 (2017) 892–897.
[14] H. Attar, et al., Nanoindentation and wear properties of Ti and Ti-TiB composite materials produced by selective laser melting, Mater. Sci. Eng., A 688 (2017) 20–26.
[15] M.L. Oyen, R.F. Cook, A practical guide for analysis of nanoindentation data, J. Mech. Behav. Biomed. Mater. 2 (4) (2009) 396–407.
[16] J.M. Wheeler, J. Michler, Invited Article, Indenter materials for high temperature nanoindentation, Rev. Sci. Instrum. 84 (10) (2013), 101301.
[17] K.D. Sattler, Handbook of Nanophysics: Functional Nanomaterials, CRC press, 2010.
[18] C.B. Carter, M.G. Norton, Ceramic Materials: Science and Engineering, vol. 716, Springer, 2007.
[19] E. Guo, et al., Mechanical properties of microconstituents in Nb-Si-Ti alloy by micropillar compression and nanoindentation, Mater. Sci. Eng., A 687 (2017) 99–106.
[20] J. Fornell, et al., Enhanced mechanical properties and in vitro corrosion behavior of amorphous and devitrified Ti40Zr10Cu38Pd12 metallic glass, J. Mech. Behav. Biomed. Mater. 4 (8) (2011) 1709–1717.
[21] X. Zhao, et al., Ti2Ni alloy: a potential candidate for hydrogen storage in nickel/metal hydride secondary batteries, Energy Environ. Sci. 3 (9) (2010) 1316–1321.
[22] F. Geng, P. Shi, D.Z. Yang, Review on the development of NiTi shape memory alloy as a biomaterial, J. Funct. Mater. 36 (1) (2005) 11–14.
[23] N.S. Stoloff, C.T. Liu, S.C. Deevi, Emerging applications of intermetallics, Intermetallics 8 (9–11) (2000) 1313–1320.
[24] B.B. Panigrahi, Sintering behaviour of Ti–2Ni and Ti–5Ni elemental powders, Mater. Lett. 61 (1) (2007) 152–155.
[25] I.M. Robertson, G.B. Schaffer, Suitability of nickel as alloying element in titanium sintered in solid state, Powder Metall. 52 (3) (2009) 225–232.
[26] R.J. Low, I.M. Robertson, G.B. Schaffer, Excessive porosity after liquid-phase sintering of elemental titanium powder blends, Scripta Mater. 56 (10) (2007) 895–898.
[27] I.M. Robertson, G.B. Schaffer, Swelling during liquid phase sintering of Ti–Ni alloys, Powder Metall. 52 (3) (2009) 213–224.
[28] H.-W. Liu, D. Paul Bishop, K.P. Plucknett, A comparison of Ti–Ni and Ti-Sn binary alloys processed using powder metallurgy, Mater. Sci. Eng., A 644 (2015) 392–404.
[29] J. Musil, et al., Relationships between hardness, Young's modulus and elastic recovery in hard nanocomposite coatings, Surf. Coating. Technol. 154 (2) (2002) 304–313.
[30] A. Leyland, A. Matthews, On the significance of the H/E ratio in wear control: a nanocomposite coating approach to optimised tribological behaviour, Wear 246 (1) (2000) 1–11.
[31] G.M. Pharr, Measurement of mechanical properties by ultra-low load indentation, Mater. Sci. Eng., A 253 (1) (1998) 151–159.
[32] X. Li, B. Bhushan, A review of nanoindentation continuous stiffness measurement technique and its applications, Mater. Char. 48 (1) (2002) 11–36.
[33] W.C. Oliver, G.M. Pharr, An improved technique for determining hardness and elastic modulus using load and displacement sensing indentation experiments, J. Mater. Res. 7 (6) (1992) 1564–1583.
[34] S. Gautham, S. Sasmal, Determination of fracture toughness of nano-scale cement composites using simulated nanoindentation technique, Theor. Appl. Fract. Mech. 103 (2019), 102275.
[35] A. Foul, et al., Dynamic transformation of α → β titanium at temperatures below the β-transus in commercially pure titanium, Mater. Sci. Eng., A 722 (2018) 156–159.
[36] A.L. Rominiyi, et al., Synthesis, microstructural and phase evolution in Ti–2Ni and Ti–10Ni binary alloys consolidated by spark plasma sintering technique, Int. J. Adv. Des. Manuf. Technol. 104 (1–4) (2019) 1041–1049.
[37] J. Liu, et al., Microstructure evolution and mechanical properties of functionally graded Fe–8Cr-xNi alloys fabricated by spark plasma sintering, Mater. Sci. Eng., A 866 (2023), 144648.
[38] A.L. Rominiyi, et al., Influence of sintering temperature on densification, microstructure and mechanical properties of Ti-6Ni alloy developed via spark plasma sintering, IOP Conf. Ser. Mater. Sci. Eng. 655 (2019), 012017.
[39] A. Fuji, Y. Horiuchi, K. Yamamoto, Friction welding of pure titanium and pure nickel, Sci. Technol. Weld. Join. 10 (3) (2005) 287–294.
[40] L. Xu, et al., In situ TiC/Ti2Ni reinforced CrTi4-based composites during laser cladding, J. Alloys Compd. 892 (2022), 162086.
[41] Y. Wang, et al., Reactive composite brazing of C/C composite and GH3044 with Ag–Ti mixed powder filler material, Mater. Sci. Eng., A 759 (2019) 303–312.
[42] C.A. Schuh, A.C. Lund, Application of nucleation theory to the rate dependence of incipient plasticity during nanoindentation, J. Mater. Res. 19 (7) (2004) 2152–2158.
[43] W. Wang, C.B. Jiang, K. Lu, Deformation behavior of Ni3Al single crystals during nanoindentation, Acta Mater. 51 (20) (2003) 6169–6180.
[44] M. Khantha, V. Vitek, D.P. Pope, Strain-rate dependent mechanism of cooperative dislocation generation: application to the brittle–ductile transition, Mater. Sci. Eng., A 319 (2001) 484–489.
[45] B. Gurrutxaga-Lerma, et al., The mechanisms governing the activation of dislocation sources in aluminum at different strain rates, J. Mech. Phys. Solid. 84 (2015) 273–292.
[46] L. Dekhil, et al., Microstructural, magnetic, and nanoindentation studies of the ball-milled Ti80Ni20 alloy, J. Supercond. Nov. Magnetism 32 (11) (2019) 3623–3636.
[47] S. Abdi, et al., Effect of Nb addition on microstructure evolution and nanomechanical properties of a glass-forming Ti–Zr–Si alloy, Intermetallics 46 (2014) 156–163.
[48] J. Zhang, G.L. Niebur, T.C. Ovaert, Mechanical property determination of bone through nano- and micro-indentation testing and finite element simulation, J. Biomech. 41 (2) (2008) 267–275.
[49] J. Thornby, et al., Indentation-based characterization of creep and hardness behavior of magnesium carbon nanotube nanocomposites at room temperature, SN Appl. Sci. 1 (7) (2019) 1–12.
[50] A.A. Elmustafa, D.S. Stone, Nanoindentation and the indentation size effect: kinetics of deformation and strain gradient plasticity, J. Mech. Phys. Solid. 51 (2) (2003) 357–381.
[51] M. Zhao, et al., Material-length-scale-controlled nanoindentation size effects due to strain-gradient plasticity, Acta Mater. 51 (15) (2003) 4461–4469.
[52] P. Zhang, S.X. Li, Z.F. Zhang, General relationship between strength and hardness, Mater. Sci. Eng., A 529 (2011) 62–73.
[53] I. Hutchings, P. Shipway, 6 - wear by hard particles, in: I. Hutchings, P. Shipway (Eds.), Tribology, second ed., Butterworth-Heinemann, 2017, pp. 165–236.
[54] J. Xu, et al., Mechanical and corrosion-resistant properties of Ti–Nb–Si–N nanocomposite films prepared by a double glow discharge plasma technique, Ceram. Int. 40 (6) (2014) 8621–8630.
[55] I. Farias, et al., Wear modes in open porosity titanium matrix composites with TiC addition processed by spark plasma sintering, Trans. Nonferrous Metals Soc. China 29 (8) (2019) 1653–1664.
[56] A.L. Rominiyi, P.M. Mashinini, Nanoindentation study of mechanical and wear properties of spark plasma sintered Ti-6Ni-xTiCN composites, Ceram. Int. 49 (2) (2023) 2194–2203.
[57] A. Hynowska, et al., Nanostructured β-phase Ti–31.0Fe–9.0Sn and sub-μm structured Ti–39.3Nb–13.3Zr–10.7Ta alloys for biomedical applications: microstructure benefits on the mechanical and corrosion performances, Mater. Sci. Eng. C 32 (8) (2012) 2418–2425.

[58] A. Hynowska, et al., Novel Ti–Zr–Hf–Fe nanostructured alloy for biomedical applications, Materials 6 (11) (2013) 4930–4945.
[59] M. Karbalaei Akbari, et al., Wear and friction behavior of nanosized TiB_2 and TiO_2 particle-reinforced casting A356 aluminum nanocomposites: a comparative study focusing on particle capture in matrix, J. Compos. Mater. 49 (29) (2015) 3665–3681.
[60] K. Kato, Wear in relation to friction—a review, Wear 241 (2) (2000) 151–157.
[61] J.F. Archard, W. Hirst, The wear of metals under unlubricated conditions, Proc. R. Soc. London, A 236 (1206) (1956) 397–410.